Nano Research
https://doi.org/10.1007/s12274-018-1992-1
Research Article
ISSN 1998-0124
CN 11-5974/O4

Triboelectric nanogenerator enhanced multilayered antibacterial nanofiber air filters for efficient removal of ultrafine particulate matter

Guang Qin Gu[1,2,§], Chang Bao Han[1,2,§], Jing Jing Tian[1,2,§], Tao Jiang[1,2], Chuan He[1,2], Cun Xin Lu[1,2], Yu Bai[1,2], Jin Hui Nie[1,2], Zhou Li[1,2] (✉), and Zhong Lin Wang[1,2,3] (✉)

[1] *Beijing Institute of Nanoenergy and Nanosystems, Chinese Academy of Sciences, Beijing 100083, China*
[2] *School of Nanoscience and Technology, University of Chinese Academy of Sciences, Beijing 100049, China*
[3] *School of Materials Science and Engineering, Georgia Institute of Technology, Atlanta, GA 30332-0245, USA*
[§] *Guang Qin Gu, Chang Bao Han, and Jing Jing Tian contribute equally to this work.*

Received: 1 December 2017
Revised: 4 January 2018
Accepted: 7 January 2018

KEYWORDS

triboelectric nanogenerator,
antibacterial property,
electrospinning,
Ag-polyimide nanofiber,
air filter,
ultrafine particle

ABSTRACT

We developed a high-efficiency rotating triboelectric nanogenerator (R-TENG)-enhanced multilayered antibacterial polyimide (PI) nanofiber air filters for removing ultrafine particulate matter (PM) from ambient atmosphere. Compared to single-layered PI nanofiber filters, the multilayered nanofiber filter can completely remove all of the particles with diameters larger than 0.54 μm and shows enhanced removal efficiency for smaller PM particles. After connecting with a R-TENG, the removal efficiency of the filer for ultrafine particles is further enhanced. The highest removal efficiency for ultrafine particulate matter is 94.1% at the diameter of 53.3 nm and the average removal efficiency reached 89.9%. Despite an increase in the layer number, the thickness of each individual layer of the film decreased, and hence, the total pressure drop of the filter decreased instead of increasing. Moreover, the nanofiber film exhibited high antibacterial activity because of the addition of a small amount of silver nanoparticles. This technology with zero ozone release and low pressure drop is appropriate for cleaning air, haze treatment, and bacterial control.

1 Introduction

Air pollution is a major public, environmental, and health issue contributing to 7 million premature deaths worldwide, annually [1, 2]. Particulate matter (PM), as one of the major airborne pollutants, has raised serious concerns in recent years [3–5]. PM is categorized by the size of the particle as coarse, fine, and ultrafine particles (UFPs) with aerodynamic diameters within 2.5–10 μm (PM10), < 2.5 μm (PM2.5), and < 0.1 μm (PM0.1), respectively. Numerous studies have demonstrated the association of long-time PM2.5 polluted air exposure

Address correspondence to Zhong Lin Wang, zlwang@gatech.edu; Zhou Li, zli@binn.cas.cn

with morbidity and mortality from respiratory and cardiovascular diseases [6–9]. Hence, the air quality index related to the concentrations of PM2.5 and PM10 is used to reflect the daily air pollution level.

However, most of the particles (73%) are in the ultrafine fraction, whereas most of the mass (82%) could be attributed to particles in the size range of 0.1 to 0.5 μm [10]. Moreover, UFPs are much more harmful to public health. Compared to PM2.5 with larger particles, UFPs have a much higher number concentration and surface area [11], enhanced oxidation capacity [12, 13], greater inflammatory potential [11], and higher pulmonary deposition efficiency [14, 15]. The UFPs cannot be filtered out by the nose and bronchioles and their small size allows them to be breathed deeply into the lungs, where they are able to penetrate alveolar epithelium and enter the pulmonary interstitium and vascular space to be absorbed directly into the blood stream [16]. The body also does not have efficient mechanisms for clearing the deeper part of the lung as only a very small fraction of natural particles would be as small as these [17]. The UFPs are highly chemically reactive owing to their small size and large surface area [18]. Further, they also carry a large amount of toxic compounds on their surfaces [19]. For example, in air emissions from incinerators, heavy metals, dioxins, hydrocarbons, and other organic chemicals can adhere to the surface of UFPs and increase their toxicity [20]. Among the various hazards of PM pollutants, microorganisms in PM2.5 and PM10 are speculated to be responsible for various allergies and for the spreading of respiratory diseases [21]. Therefore, it is necessary to develop air filters to remove these UFPs and microorganisms for the sake of people's health.

Nowadays, electrostatic precipitation and fibrous filters are widely utilized to remove PMs. One major drawback of the electrostatic precipitators is that they inevitably ionize air, and hence produce ozone [22], which causes negative effects on human health with the possibility of causing cancer [23, 24]. As for fibrous filters, they present the advantage of high efficiency to remove particles larger than their holes. However, the removal efficiency for UFPs, whose diameters are much smaller than the holes of the fibrous filter, decreases significantly. Moreover, the pressure drop increases with dust loading [25, 26].

Nanogenerators, in particular, piezoelectric nanogenerators [27–29] and triboelectric nanogenerators (TENGs) [30–34], were invented by Wang's group in 2006 [35] and 2012 [36], respectively. TENGs, based on triboelectrification and electrostatic induction effects, were invented to harvest energies from all kinds of mechanical movements such as human motion, wind, water wave [37–42]. One of the greatest advantages of TENG is the generation of a high open-circuit voltage (V_{OC}), which is generally hundreds of times higher than that generated by electromagnetic generators [43]. For example, a TENG based on collision between polytetrafluoroethylene (PTFE) pellets and electrodes can yield a space electric field as high as 12 MV/m and a self-powered triboelectric filter based on this TENG shows a removal efficiency of ~ 95.5% for PM2.5 [44]. Furthermore, the high voltage of TENGs does not ionize the surrounding air, and therefore, no ozone is produced.

In our previous study, a rotating triboelectric nanogenerator (R-TENG)-enhanced electrospinning nanofiber film filter was fabricated for efficient PM removal [45]. However, only a single layer of charged nanofiber film cannot provide adequately high removal efficiency for ultrafine particulate matters. Moreover, the threat of microorganisms such as bacteria to human health is not considered. In this study, we developed a high-efficiency R-TENG-enhanced multilayered antibacterial polyimide (PI) nanofiber air filters for the removal of ultrafine PM and microorganisms in ambient atmosphere. Compared with the single-layered nanofiber filter, the multilayered nanofiber filter can remove all of the particles with diameters larger than 0.54 μm and show enhanced removal efficiency for smaller PM particles. After connecting with the R-TENG, the removal efficiencies for ultrafine particles are further enhanced. The highest removal efficiency for ultrafine particulate matter is 94.1% at the diameter of 53.3 nm and the average removal efficiency reached 89.9%. Although the layer number was increased, the thickness of each layer of the films decreased, and hence, the total pressure drop of the filter did not increase, but decreased. Moreover, the nanofiber film exhibited high antibacterial activity because of a small amount of silver nanoparticles incorporated in it. This technology with zero ozone release and low pressure drop is effective for cleaning air, haze treatment, and bacterial control.

2 Experimental section

2.1 Electrospinning

The solution used for electrospinning was a polyamide acid (PAA) solution in dimethylformamide (DMF) with a solid content of ~ 15.5 wt.%. Silver nitrate was first dissolved in DMF and then added to the polymer solution, keeping the Ag ratio at 3 wt.% in the final Ag-polyimide (PI) nanofiber. A 5 mL syringe with a 22-gauge needle tip was used to load the polymer solution. A syringe pump (model LSP01-1A, Longer Pump) was used to pump the solution out of the needle tip. The electrospinning nanofibers were collected by a 100 mesh stainless-steel wire mesh. The voltage applied between the needle tip and the mesh was 18 kV. During electrospinning, the nanofibers lay across the mesh holes to form the air filter.

2.2 Antibacterial test

A fresh bacterial solution was first acquired by culturing *E. coli* and *S. aureus* in an autoclaved lysogenic broth (LB) medium overnight at 37 °C (bacteria were in the stationary phase); the rotation speed was 120 rpm. Subsequently, 1 mL of the *E. coli* and *S. aureus* solution was pipetted from the phase incubated overnight into another flask containing 100 mL of fresh LB. The mixture was then cultured at 37 °C for another 5 h to obtain a bacterial suspension at the exponential growth phase. Thereafter, the bacterial suspension was centrifuged at 10,000 rpm to separate the bacteria from the culture medium, and then the bacteria were washed and resuspended in a sterilizing saline to achieve a concentration of ~ 10^6 colony-forming units (CFU)/mL for the sterilization test.

2.3 PM generation and evaluation of the filtering efficiency

The PM generation and efficiency measurements were performed in a 30 m^3 lab. The PM particles used in this work were generated by burning cigarette. The PM particles from cigarette smoke had a wide particle size distribution ranging from < 10 nm to > 10 μm. By diluting the smoke PM by air and waiting for 30 min to allow an even dispersion of the smoke in the air, the inflow concentration was controlled to a hazardous pollution level equivalent to the PM2.5 index > 300. A handheld particle counter (3016-IAQ, Lighthouse), a scanning mobility particle sizer (SMPS 3938L75, TSI), and an aerodynamic particle sizer (3321, TSI) were used to detect the PM particle number concentration before and after filtration. The removal efficiency was calculated by comparing the number concentration before and after filtration.

2.4 Pressure drop and estimation of ozone

The pressure drop was measured using a differential pressure gauge (Testo 510) and the gas velocity was measured by an anemometer (Testo 450-V1). Ozone was analyzed by an ozone monitor (aeroQUAL, series 200).

2.5 Characterization

Field emission scanning electron microscopy (FE-SEM) images were obtained using FEI Nova NANOSEM 450 SEM with an acceleration voltage of 5 kV for imaging. The open-circuit voltage was determined using an oscilloscope (DSO-X 2014A; Agilent). The absorbance spectrum of Ag nanoparticles dissolved in DMF was recorded on an ultraviolet–visible–near infrared (UV–vis–NIR) spectrophotometer (UV 3600).

3 Results and discussion

The fabrication of the antibacterial PI air filter by electrospinning is schematically illustrated in Fig. 1(a). A given quantity of silver nitrate was first dissolved in DMF. Then, the resulting solution was added to a solution of PAA, to obtain an electrospinning solution. Further details could be found in the Experimental section. As reported previously, DMF reacted with silver nitrate, forming Ag nanoparticles according to Eq. (1) [46, 47]

$$HCONMe_2 + 2Ag^+ + H_2O \rightarrow 2Ag + Me_2NCOOH + 2H^+ \quad (1)$$

UV–vis absorbance spectrum of the Ag nanoparticles in DMF solution is shown in Fig. S1 in the Electronic Supplementary Material (ESM). The plasmon peak of Ag nanoparticles is observed at 430 nm. Figure 1(b) shows the energy dispersive spectrum (EDS) patterns of PI nanofibers and silver nanoparticle-doped

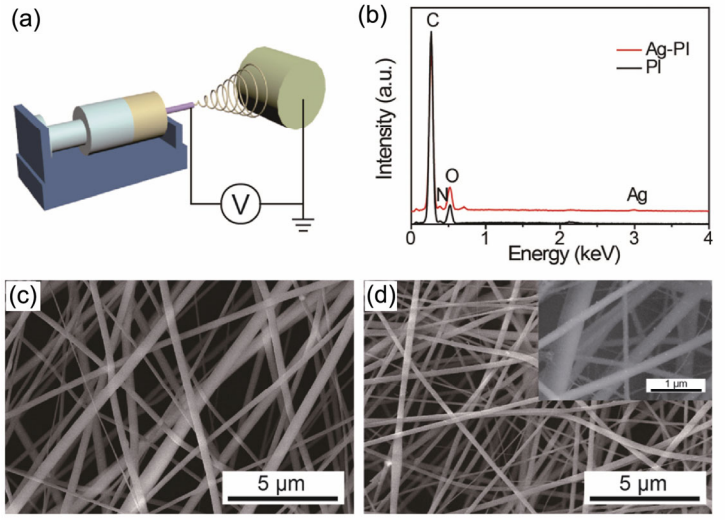

Figure 1 (a) Schematic of the fabrication of a PI air filter by electrospinning. (b) EDS spectra of PI and Ag-PI films. (c) and (d) FE-SEM image of pure PI and Ag-PI nanofibers. Inset of (d) shows the FE-SEM image of Ag-PI at a large magnification.

PI (Ag-PI) nanofibers; the weight ratio of silver in the latter is 3 wt.%. The results clearly indicate the existence of silver in the Ag-PI nanofiber film. Figures 1(c) and 1(d) show the FE-SEM images of the PI and Ag-PI nanofibers, respectively. The Ag-PI nanofibers have a smaller diameter on average. The reason is that, after the addition of silver nitrate, the content of the electrolyte in the solution increases which in turn increases the electrostatic force on the nanofibers during the electrospinning process [48]. The inset of Fig. 1(d) shows the FE-SEM image of Ag-PI nanofibers at a larger magnification and Ag nanoparticles are clearly observed on the surface of Ag-PI nanofibers.

To evaluate the PM removal performance of the as-prepared Ag-PI nanofiber filters, we designed a measurement setup, as shown in Fig. 2(a). Ag-PI nanofiber films were placed inside a square acrylic tube and connected with the filtration performance testing system. The Ag-PI nanofiber films were separated by acrylic spacers as shown in Fig. 2(b). The thickness of the spacer is 2 mm. A pressure gauge was used to test the pressure drop at different gas flows for all the Ag-PI nanofiber filters. A PM particle counter was used to measure the particle number concentration in the dusty air before and after filtering. The PM particles used in this study were generated by burning cigarettes. This is a good model system for air filtration since it contains a wide range of PM particles with various sizes [45, 48]. A R-TENG was used to charge the Ag-PI nanofiber films; this is mainly composed of a rotator and a stator, as shown in Fig. 2(a). The rotator rotates under the driving force from a motor, while the stator is fixed on the motor. The working principle of this kind of R-TENG has been reported previously [49, 50]. Output signals of R-TENG were first rectified through a rectifier bridge and then connected to the stainless-steel mesh of the Ag-PI nanofiber film. The rectified voltage of the R-TENG is shown in Fig. 2(c). The rectified voltage is ~ 480 V and some peaks can reach 1,000 V. To demonstrate that the Ag-PI film can be charged by the R-TENG, the surface electrostatic potential of the Ag-PI nanofiber film was determined, and the results are shown in Fig. 2(d). As shown, when the R-TENG was operated, the surface electrostatic potential of the Ag-PI film increased to a value as high as 550 V.

For the particulate filter, the basic filtration mechanism includes mechanical filtration, electrostatic filtration, and chemisorption. In the mechanical filtration, interception, inertial impaction, diffusion, and gravitational settling are the main mechanisms responsible for the removal of particles [51, 52]. In general, a majority of the nanoparticles can be removed by diffusion, whereas particles within the size range of sub-micron to several microns are substantially reduced by interception [53]. For particles with sizes of tens of microns, inertial impaction and gravitational settling become critical. Through the electrostatic effect, the electrostatic filtration can remove particles with large sizes ranging from

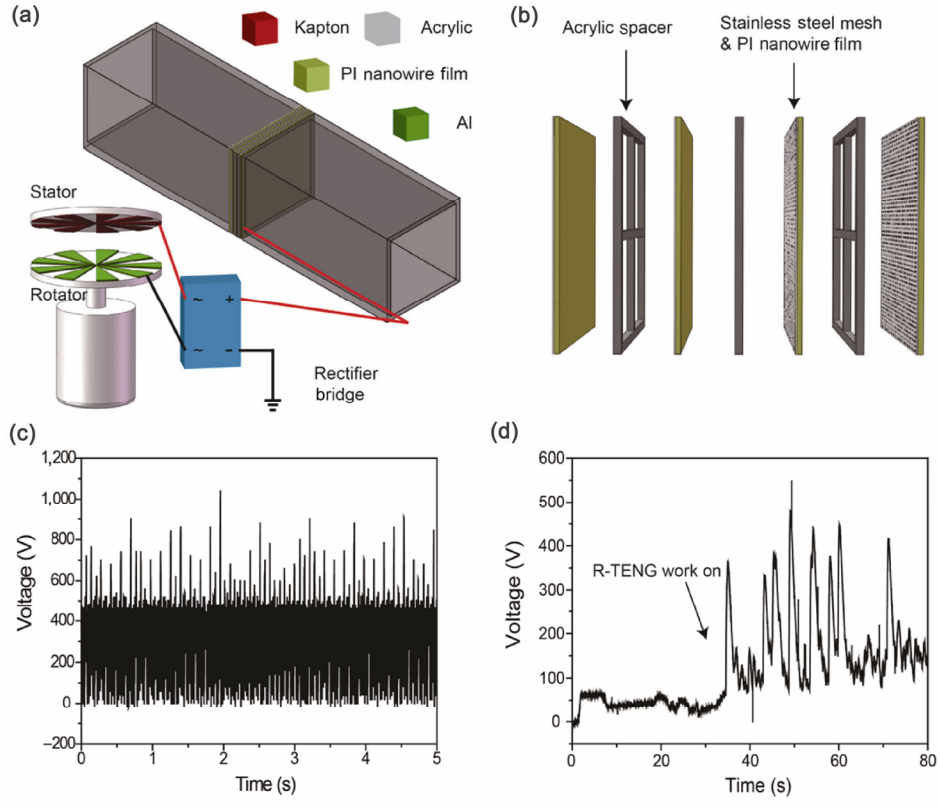

Figure 2 (a) Schematic illustration of the setup used for PM removal efficiency measurement. (b) The diagram of PI nanofiber films and spacers assembled. (c) The rectified voltage of the R-TENG. (d) The surface potential of the Ag-PI nanofiber film before and after operating with the R-TENG.

nanoparticles to micro-particles. For example, more than 97% removal efficiency for the particle size ranging from dozens of nanometers to ten micrometers has been realized by the electrostatic precipitator [54]. Based on the filtration mechanisms, the removal efficiencies of the particles with different sizes are schematically shown in Fig. 3(a). In our experiment, the Ag-PI nanofiber films were positive charged by the R-TENG. Together with the electrostatic effect, particles ranging from nanometers to tens of micrometers can be effectively removed, as shown in Fig. 3(b). Consequently, the removal efficiency of the Ag-PI nanofiber filter increases notably, especially for particles with a diameter smaller than 500 nm, which could pass through the holes of the nanofiber filter. Figures 3(c) and 3(d) show the FE-SEM images of the Ag-PI nanofiber film before and after the filtration of PM particles. As reported by Cui's group [55], at the initial capture stage, PM is captured by the Ag-PI nanofibers and is bound tightly on the nanofibers. As more smoke is fed continuously to the filter, more PM particles are attached. The particles are able to move along the Ag-PI nanofibers and they aggregate to form larger particles. As the capture proceeds further, the Ag-PI filters are filled with large aggregated PM particles. The junction of nanofibers had more PM accumulated and formed spherical particles of larger sizes. Eventually, it seems that the PM particles formed a layer attached on the PI nanofibers, as shown in Fig. 3(d).

The PM2.5 removal efficiencies of the filters with a single layer of the Ag-PI nanofiber film based on particle counts at different electrospinning time are shown in Fig. 4(a). It is obvious that as the electrospinning time increases, the removal efficiency of the filters also increases. After connecting the R-TENG, the removal efficiency of all filters is further increased. The removal efficiencies of the filter with single-layered electrospun Ag-PI nanofiber film in 60 min for PM0.3, PM0.5, PM1.0, PM2.5, PM5.0, and PM10 were determined, and the results are shown in Fig. 4(b). The removal efficiency increases as the PM diameter increases. This demonstrates

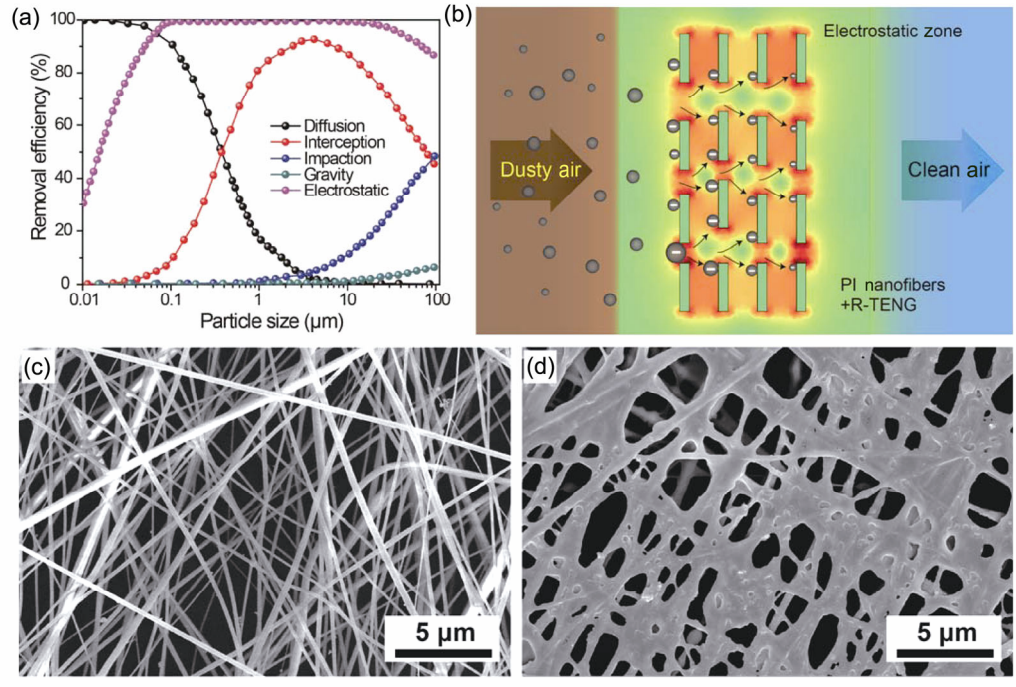

Figure 3 (a) Filtering mechanism and the PM removal efficiency of the triboelectric filter. (b) Schematic of the filtration mechanism of the filter. SEM image of the Ag-PI nanofibers (c) before filtration and (d) after filtration.

that the nanofiber film shows a high removal efficiency for PM particles with diameters larger than its holes.

The removal efficiencies of the filter with different layers of nanofiber films obtained in 10 min with and without R-TENG are shown in Fig. 4(c). As shown, the removal efficiency increases as the number of layers increases. Upon connecting the R-TENG, the removal efficiency is further enhanced. To verify the effect of film spacing on the filtration efficiency, PM2.5 removal efficiencies of two-layered electrospun films obtained in 20 min under different film spacing were tested, as shown in Fig. S2 in the ESM. Different film spacing is achieved by using many acrylic spacers, the thickness of each spacer is 1 mm. As shown, the removal efficiency remains almost the same as the spacing increases from 1 to 4 mm. The removal efficiencies of the filter with three-layered electrospun Ag-PI nanofiber films in 10 min for PM0.3, PM0.5, PM1.0, PM2.5, PM5.0, and PM10 were determined and the results are shown in Fig. 4(d). As shown, for PM particles larger than 0.5 μm in diameter, the removal efficiency is higher than 90%. Upon connecting the R-TENG, all the removal efficiencies were enhanced, especially for PM0.3, which shows the significance of electrostatic precipitation. To demonstrate the stability of the removal efficiency of the multilayered Ag-PI nanofiber filter, PM2.5 removal efficiencies of the filter with three-layered Ag-PI nanofiber films obtained in 10 min with and without R-TENG under different gas flows are shown in Fig. 4(e). The removal efficiency is further increased after connecting with the R-TENG and it remains almost the same as the gas flow is increased from 12 to 60 L/min. The pressure drops of the filter with different layers of nanofiber films are shown in Fig. 4(f). The pressure drop for filters of three-layered films was only 50 Pa at the gas flow of 60 L/min.

The distributions of particle number in dusty air, after filtering and after R-TENG-enhanced filtering (with three-layered Ag-PI nanofiber films obtained in 10 min), for sizes ranging from 0.54 to 20 μm are shown in Fig. 5(a) and the corresponding removal efficiencies are shown in Fig. 5(b). The removal efficiencies of the filter for particles in this range are 100%, which demonstrates that our filter is highly efficient for the removal of PM particles with a diameter larger than 0.54 μm, which agrees with the results shown in Fig. 4(d). The distributions of the particle numbers in dusty air, after filtering and after R-TENG-enhanced filtering (with three-layered Ag-PI nanofiber films obtained in

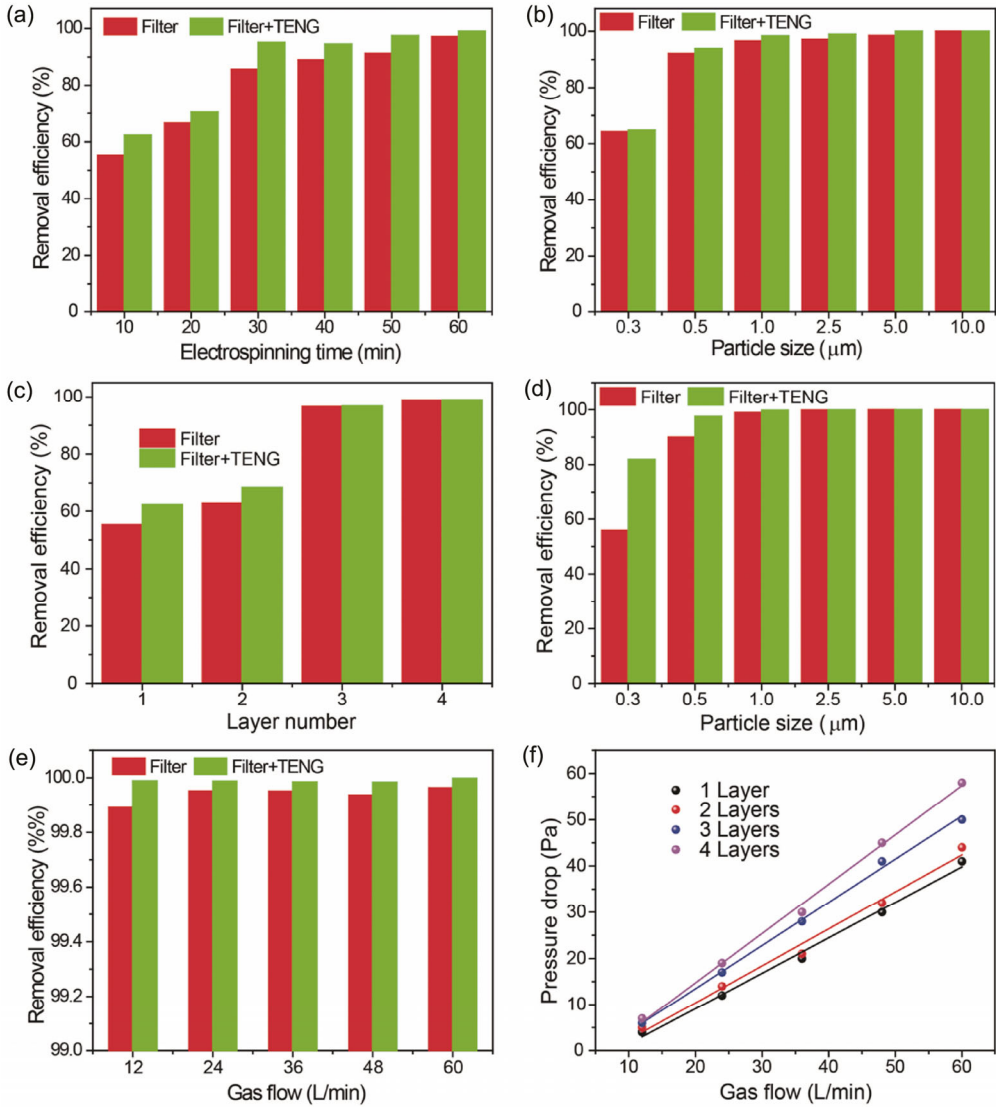

Figure 4 (a) PM2.5 particle number removal efficiencies of different single-layered filters with and without R-TENG. (b) Removal efficiencies of particle numbers of different-sized PMs using single-layered 60 min electrospun film with and without R-TENG. (c) PM2.5 removal efficiencies by particle counts for filters with different layer numbers of the Ag-PI nanofiber films obtained in 10 min with and without R-TENG. (d) Removal efficiencies of particle numbers for different-sized PMs of the filter with three-layered electrospun films obtained in 10 min with and without R-TENG. (e) PM2.5 removal efficiencies of the filter with three-layered electrospun films obtained in 10 min with and without R-TENG under different gas flows. (f) Pressure drop of filters with different layer number of electrospun films obtained in 10 min under different gas flows.

10 min), for sizes ranging from 15 to 550 nm are shown in Fig. 5(c) and the corresponding removal efficiencies are shown in Fig. 5(d). As shown, the particle number of these particles is in the range of 10^5 in dusty air. After passing through the Ag-PI nanofiber filter, ~ 80% of the particles are filtered. The highest removal efficiency is 89.8% for the PM diameter of 51.4 nm. After connecting with the R-TENG, the removal efficiency was further enhanced and ~ 90% of the particles are filtered. The highest removal efficiency reached 94.1% at the PM diameter of 53.3 nm. The removal efficiency for UFPs increased from 83.5% to 89.9% after connecting with the R-TENG. It can be observed that the curve of the removal efficiency is similar to the curve of the electrostatic effect, as shown in Fig. 3(a). This is because, in the submicron region, the main removal mechanism is electrostatic precipitation. Compared with the single-layered R-TENG-enhanced filter previously reported by us [45], not only the highest removal efficiency is increased, but also the range of

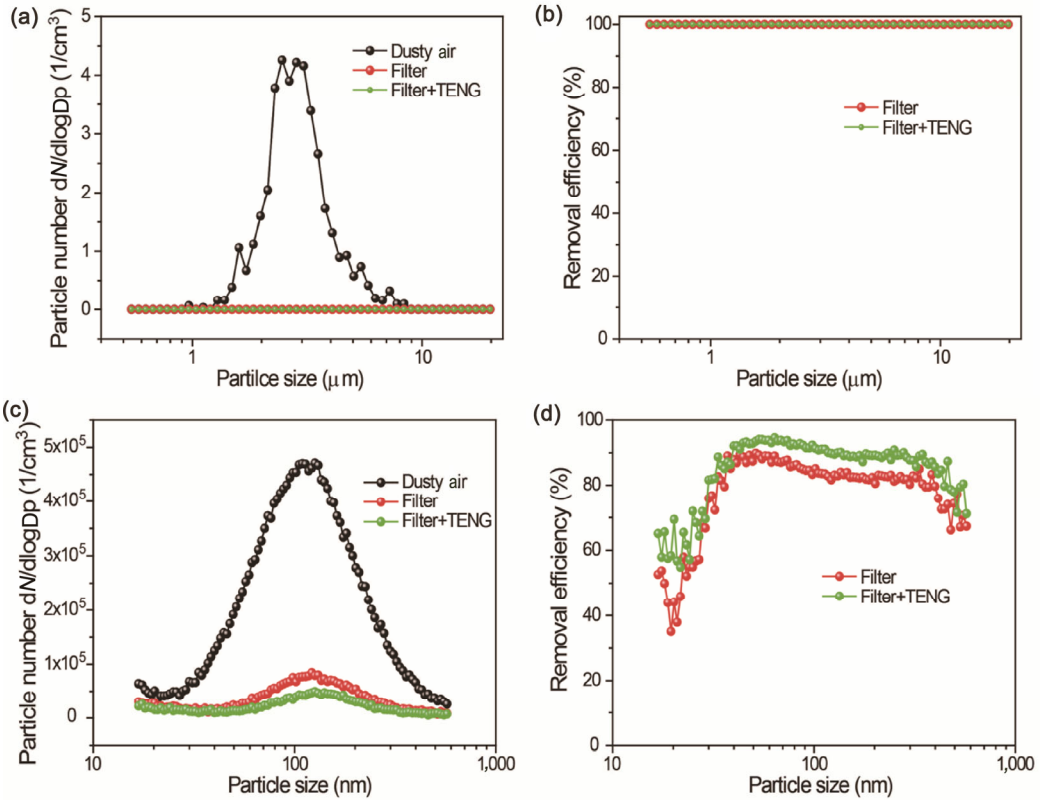

Figure 5 (a) Particle size distribution of the particulates in dusty air, after simple filtering and after R-TENG-enhanced filtering, in the diameter range of 0.54–20 nm. (b) Comparison of the removal efficiency of the filter with and without R-TENG, in the diameter range of 0.54–20 nm. (c) Particle size distribution of the particulates in the dusty air, after filtering and after R-TENG-enhanced filtering, in the diameter range of 15–550 μm. (d) Comparison of the removal efficiency of the filter with and without R-TENG in the diameter range of 15–550 μm. The filter used here consists of three-layered electrospun films obtained in 10 min.

the filtration efficiency at higher than 90% is enlarged enormously, where the range of 30 to 41.4 nm is enlarged to the range of 40.0 to 135.8 nm. These results suggest that the multilayered R-TENG-enhanced Ag-PI nanofiber filters have better removal efficiency for nanoparticles.

The antibacterial effect of the electrospun PI films was investigated using *Escherichia coli* (*E. coli*) and *staphylococcus aureus* (*S. aureus*), which are the model gram-negative and gram-positive bacteria, respectively [56, 57]. The bacterial suspension at the exponential growth phase was first obtained by culturing it at 37 ℃ in an incubator shaker for further 5 h, and then, the bacteria suspension (*E. coli* or *S. aureus*) was diluted with the sterilizing saline culture medium to 10^6 CFU/mL. The PI and Ag-PI nanofibers (Φ = 1.2 cm) were immersed in a bacterial suspension (10 mL) comprising 1 mL of 10^6 CFU/mL suspension and 9 mL of sterilizing saline, and shook in an incubator shaker at 120 rpm and 37 ℃ for 30 h. A CFU counting method was used to estimate the number of viable *E. coli* and *S. aureus* remaining in the suspensions. Figures 6(a) and 6(b) show the FE-SEM images of the *E. coli* and *S. aureus* cell on the Ag-PI nanofibers after co-culturing for 30 h. We can observe that the holes of the Ag-PI nanofibers are much smaller than the diameter of the bacteria, demonstrating that the Ag-PI nanofiber filter can effectively filter these bacteria. As shown in Figs. 6(c)–6(f), the CFU of *E. coli* and *S. aureus* remaining in the suspensions were counted. 94.6% of *E. coli* and 98.5% of *S. aureus* were killed, demonstrating the good antibacterial property of the Ag-PI film. As for the mechanism of antibacterial activity, one of the cytotoxic mechanism is the uptake of Ag nanoparticles by the bacterial cells as they are able to penetrate the bacterial cell wall, which cause DNA damage and enzyme inhibition. Other cytotoxicity mechanism may arise from the presence of oxidatively released Ag ions from the nanoparticle surface [58]. The exposition of

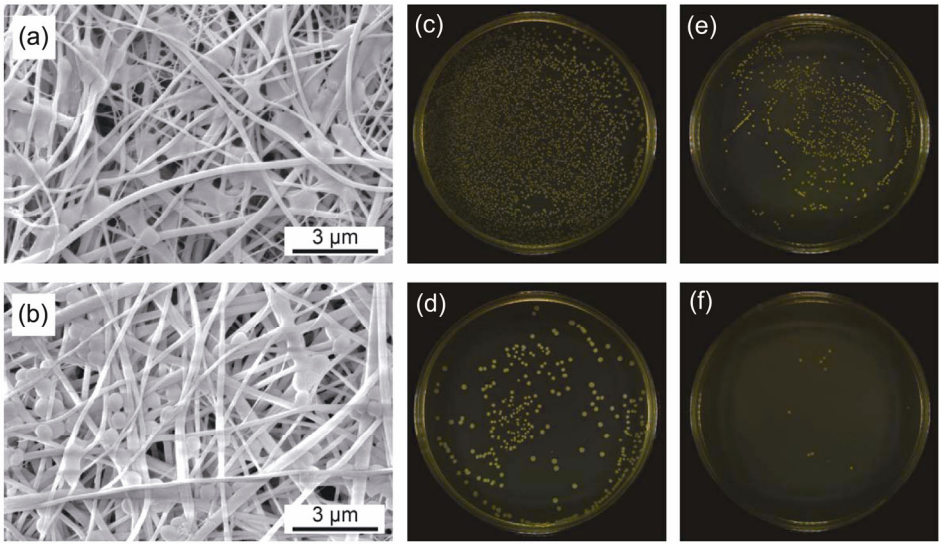

Figure 6 FE-SEM images of (a) *E. coli* and (b) *S. aureus* on the Ag-PI nanowire film. Photographs of *E. coli* colonies after co-culturing for 30 h with a (c) PI nanofiber film and (d) Ag-PI film. Photographs of *S. aureus* colonies after co-culturing for 30 h with (e) PI nanofiber film and (f) Ag-PI film.

bacterial cells to silver ions induces changes in the cell membrane structural constituents, leading to the enhancement of its permeability and damage. This can affect the transport of electrolytes and other metabolites, leading to the alteration of basic cell functions and finally cell death [59–61].

Finally, an ozone monitor was used to test if ozone was produced. No ozone was detected during the 1 h testing process. We can analyze it in the context of the working mechanism of TENG. TENG works by the coupling of triboelectrification and electrostatic induction effect. The tribo-charges generated are static charges that would remain in the triboelectric layer/materials, and therefore, there is no production of ozone.

4 Conclusion

In this paper, we developed a high-efficiency R-TENG-enhanced multilayered PI nanofiber air filter for the removal of UFPs from ambient atmosphere. Compared with the single-layered nanofiber filter, the multilayered nanofiber filter can remove all the particles with diameters larger than 0.54 μm. After connecting with the R-TENG, the removal efficiency of the filter for ultrafine particles was further enhanced. The highest removal efficiency for ultrafine particulate matter was 94.1% at the diameter of 53.3 nm and the average removal efficiency reached 89.9%. Although the layer number increased, the thickness of each layer of the films decreased, and hence, the total pressure drop of the filter did not increase; instead, it decreased. Moreover, the nanofiber film exhibited high antibacterial activity due to the small amount of silver nanoparticles added. This technology with zero ozone release and low pressure drop is suitable for air cleaning, haze treatment, and bacterial control.

Acknowledgements

Supports from the "thousands talents" program for the pioneer researcher and his innovation team, the National Key R & D Project from Ministry of Science and Technology (No. 2016YFA0202704), National Natural Science Foundation of China (Nos. 51432005, 51608039, 5151101243, 51561145021, 51702018, and 51505457), China Postdoctoral Science Foundation (No. 2015M581041), Natural Science Foundation of Beijing, China (No. 4154090), and Beijing Municipal Science & Technology Commission (No. Z171100000317001) are appreciated.

Electronic Supplementary Material: Supplementary material (Fig. S1 shows the absorbance spectrum of the Ag nanoparticles, Fig. S2 shows PM2.5 removal efficiencies of R-TENG enhanced two-layer 20 min electrospinning films under different film spacing) is available in the online version of this article at https://doi.org/10.1007/s12274-018-1992-1.

References

[1] World Health Organization. 7 million premature deaths annually linked to air pollution. http://www.who.int/mediacentre/news/releases/2014/air-pollution/en/ (accessed on Mar 29, 2017).

[2] Newby, D. E.; Mannucci, P. M.; Tell, G. S.; Baccarelli, A. A.; Brook, R. D.; Donaldson, K.; Forastiere, F.; Franchini, M.; Franco, O. H.; Graham, I. et al. Expert position paper on air pollution and cardiovascular disease. *Eur. Heart J.* **2015**, *36*, 83–93.

[3] Zhang, R.; Jing, J.; Tao, J.; Hsu, S. C.; Wang, G.; Cao, J.; Lee, C. S. L.; Zhu, L.; Chen, Z.; Zhao, Y. et al. Chemical characterization and source apportionment of $PM_{2.5}$ in Beijing: Seasonal perspective. *Atmos. Chem. Phys.* **2013**, *13*, 7053–7074.

[4] Nel, A. Air pollution-related illness: Effects of particles. *Science* **2005**, *308*, 804–806.

[5] Harrison, R. M.; Yin, J. X. Particulate matter in the atmosphere: Which particle properties are important for its effects on health? *Sci. Total Environ.* **2000**, *249*, 85–101.

[6] Brook, R. D.; Franklin, B.; Cascio, W.; Hong, Y. L.; Howard, G.; Lipsett, M.; Luepker, R.; Mittleman, M.; Samet, J.; Smith, S. C. et al. Air pollution and cardiovascular disease: A statement for healthcare professionals from the expert panel on population and prevention science of the American Heart Association. *Circulation* **2004**, *109*, 2655–2671.

[7] Brook, R. D.; Rajagopalan, S.; Pope, C. A.; Brook, J. R.; Bhatnagar, A.; Diez-Roux, A. V.; Holguin, F.; Hong, Y. L.; Luepker, R. V.; Mittleman, M. A. et al. Particulate matter air pollution and cardiovascular disease: An update to the scientific statement from the American Heart Association. *Circulation* **2010**, *121*, 2331–2378.

[8] Pope, C. A.; Dockery, D. W. Health effects of fine particulate air pollution: Lines that connect. *J. Air Waste Manage. Assoc.* **2006**, *56*, 709–742.

[9] Dockery, D. W.; Pope, C. A.; Xu, X. P.; Spengler, J. D.; Ware, J. H.; Fay, M. E.; Ferris, B. G., Jr.; Speizer, F. E. An association between air pollution and mortality in six U.S. cities. *N. Engl. J. Med.* **1993**, *329*, 1753–1759.

[10] Peters, A.; Wichmann, H. E.; Tuch, T.; Heinrich, J.; Heyder, J. Respiratory effects are associated with the number of ultrafine particles. *Am. J. Respir. Crit. Care Med.* **1997**, *155*, 1376–1383.

[11] Oberdorster, G.; Gelein, R. M.; Ferin, J.; Weiss, B. Association of particulate air-pollution and acute mortality: Involvement of ultrafine particles. *Inhal. Toxicol.* **1995**, *7*, 111–124.

[12] Brown, D. M.; Wilson, M. R.; MacNee, W.; Stone, V.; Donaldson, K. Size-dependent proinflammatory effects of ultrafine polystyrene particles: A role for surface area and oxidative stress in the enhanced activity of ultrafines. *Toxicol. Appl. Pharmacol.* **2001**, *175*, 191–199.

[13] Li, N.; Sioutas, C.; Cho, A.; Schmitz, D.; Misra, C.; Sempf, J.; Wang, M. Y.; Oberley, T.; Froines, J.; Nel, A. Ultrafine particulate pollutants induce oxidative stress and mitochondrial damage. *Environ. Health Perspect.* **2003**, *111*, 455–460.

[14] Chalupa, D. C.; Morrow, P. E.; Oberdörster, G.; Utell, M. J.; Frampton, M. W. Ultrafine particle deposition in subjects with asthma. *Environ. Health Perspect.* **2004**, *112*, 879–882.

[15] Daigle, C. C.; Chalupa, D. C.; Gibb, F. R.; Morrow, P. E.; Oberdörster, G.; Utell, M. J.; Frampton, M. W. Ultrafine particle deposition in humans during rest and exercise. *Inhal. Toxicol.* **2003**, *15*, 539–552.

[16] Stearns, R. C.; Murthy, G. G. K.; Skornik, W.; Hatch, V.; Katler, M.; Godleski, J. J. Detection of ultrafine copper oxide particles in the lungs of hamsters by electron spectroscopic imaging. In: *Proceedings of ICEM 13-PARIS*. Paris, France, **1994**, 763–764.

[17] Terzano, C.; Di Stefano, F.; Conti, V.; Graziani, E.; Petroianni, A. Air pollution ultrafine particles: Toxicity beyond the lung. *Eur. Rev. Med. Pharmacol. Sci.* **2010**, *14*, 809–821.

[18] Maynard, R. L.; Howard, V. *Particulate Matter: Properties and Effects upon Health*; BIOS Scientific Publishers Ltd.: Oxford, 1999; pp 63–84.

[19] Carero, A. D. P.; Hoet, P. H. M.; Verschaeve, L.; Schoeters, G.; Nemery, B. Genotoxic effects of carbon black particles, diesel exhaust particles, and urban air particulates and their extracts on a human alveolar epithelial cell line (A549) and a human monocytic cell line (THP-1). *Environ. Mol. Mutagen.* **2001**, *37*, 155–163.

[20] QUARG. Airborne Particulate Matter in the United Kingdom. Third Report of the Quality of Urban Air Review Group, Department of the Environment. 1996.

[21] Cao, C.; Jiang, W. J.; Wang, B. Y.; Fang, J. H.; Lang, J. D.; Tian, G.; Jiang, J. K.; Zhu, T. F. Inhalable microorganisms in Beijing's $PM_{2.5}$ and PM_{10} pollutants during a severe smog event. *Environ. Sci. Technol.* **2014**, *48*, 1499–1507.

[22] Poppendieck, D. G.; Rim, D.; Persily, A. K. Ultrafine particle removal and ozone generation by in-duct electrostatic precipitators. *Environ. Sci. Technol.* **2014**, *48*, 2067–2074.

[23] Bo, Z.; Yu, K. H.; Lu, G. H.; Mao, S.; Chen, J. H.; Fan, F. G. Nanoscale discharge electrode for minimizing ozone emission from indoor corona devices. *Environ. Sci. Technol.* **2010**, *44*, 6337–6342.

[24] Chen, J. H.; Davidson, J. H. Ozone production in the negative DC corona: The dependence of discharge polarity. *Plasma Chem. Plasma Process.* **2003**, *23*, 501–518.

[25] Hosseini, S. A.; Tafreshi, H. V. 3-D simulation of particle filtration in electrospun nanofibrous filters. *Powder Technol.* **2010**, *201*, 153–160.

[26] Thomas, D.; Penicot, P.; Contal, P.; Leclerc, D.; Vendel, J. Clogging of fibrous filters by solid aerosol particles: Experimental and modelling study. *Chem. Eng. Sci.* **2001**, *56*, 3549–3561.

[27] Dagdeviren, C.; Joe, P.; Tuzman, O. L.; Park, K.-I.; Lee, K. J.; Shi, Y.; Huang, Y. G.; Rogers, J. A. Recent progress in flexible and stretchable piezoelectric devices for mechanical energy harvesting, sensing and actuation. *Extreme Mech. Lett.* **2016**, *9*, 269–281.

[28] Zhang, Y.; Yan, X. Q.; Yang, Y.; Huang, Y. H.; Liao, Q. L.; Qi, J. J. Scanning probe study on the piezotronic effect in ZnO nanomaterials and nanodevices. *Adv. Mater.* **2012**, *24*, 4647–4655.

[29] Zhang, Y.; Yang, Y.; Gu, Y. S.; Yan, X. Q.; Liao, Q. L.; Li, P. F.; Zhang, Z.; Wang, Z. Z. Performance and service behavior in 1-D nanostructured energy conversion devices. *Nano Energy* **2015**, *14*, 30–48.

[30] Liang, Q. J.; Zhang, Q.; Yan, X. Q.; Liao, X. Q.; Han, L. H.; Yi, F.; Ma, M. Y.; Zhang, Y. Recyclable and green triboelectric nanogenerator. *Adv. Mater.* **2017**, *29*, 1604961.

[31] Ma, M. Y.; Zhang, Z.; Liao, Q. L.; Zhang, G. J.; Gao, F. F.; Zhao, X.; Zhang, Q.; Xun, X. C.; Zhang, Z. M.; Zhang, Y. Integrated hybrid nanogenerator for gas energy recycle and purification. *Nano Energy* **2017**, *39*, 524–531.

[32] Wang, H. S.; Jeong, C. K.; Seo, M. H.; Joe, D. J.; Han, J. H.; Yoon, J. B.; Lee, K. J. Performance-enhanced triboelectric nanogenerator enabled by wafer-scale nanogrates of multistep pattern downscaling. *Nano Energy* **2017**, *35*, 415–423.

[33] Yi, F.; Wang, X. F.; Niu, S. M.; Li, S. M.; Yin, Y. J.; Dai, K. R.; Zhang, G. J.; Lin, L.; Wen, Z.; Guo, H. Y. et al. A highly shape-adaptive, stretchable design based on conductive liquid for energy harvesting and self-powered biomechanical monitoring. *Sci. Adv.* **2016**, *2*, e1501624.

[34] Zhang, Q.; Liang, Q. J.; Liao, Q. L.; Yi, F.; Zheng, X.; Ma, M. Y.; Gao, F. F.; Zhang, Y. Service behavior of multifunctional triboelectric nanogenerators. *Adv. Mater.* **2017**, *29*, 1606703.

[35] Wang, Z. L.; Song, J. H. Piezoelectric nanogenerators based on zinc oxide nanowire arrays. *Science* **2006**, *312*, 242–246.

[36] Fan, F. R.; Tian, Z. Q.; Wang, Z. L. Flexible triboelectric generator! *Nano Energy* **2012**, *1*, 328–334.

[37] Gu, G. Q.; Han, C. B.; Tian, J. J.; Lu, C. X.; He, C.; Jiang, T.; Li, Z.; Wang, Z. L. Antibacterial composite film-based triboelectric nanogenerator for harvesting walking energy. *ACS Appl. Mater. Interfaces* **2017**, *9*, 11882–11888.

[38] Zhu, G.; Bai, P.; Chen, J.; Wang, Z. L. Power-generating shoe insole based on triboelectric nanogenerators for self-powered consumer electronics. *Nano Energy* **2013**, *2*, 688–692.

[39] Xie, Y. N.; Wang, S. H.; Lin, L.; Jing, Q. S.; Lin, Z. H.; Niu, S. M.; Wu, Z. Y.; Wang, Z. L. Rotary triboelectric nanogenerator based on a hybridized mechanism for harvesting wind energy. *ACS Nano* **2013**, *7*, 7119–7125.

[40] Zhu, G.; Su, Y. J.; Bai, P.; Chen, J.; Jing, Q. S.; Yang, W. Q.; Wang, Z. L. Harvesting water wave energy by asymmetric screening of electrostatic charges on a nanostructured hydrophobic thin-film surface. *ACS Nano* **2014**, *8*, 6031–6037.

[41] Han, C. B.; Du, W. M.; Zhang, C.; Tang, W.; Zhang, L. M.; Wang, Z. L. Harvesting energy from automobile brake in contact and non-contact mode by conjunction of triboelectrication and electrostatic-induction processes. *Nano Energy* **2014**, *6*, 59–65.

[42] Yang, W. Q.; Chen, J.; Jing, Q. S.; Yang, J.; Wen, X. N.; Su, Y. J.; Zhu, G.; Bai, P.; Wang, Z. L. 3D stack integrated triboelectric nanogenerator for harvesting vibration energy. *Adv. Funct. Mater.* **2014**, *24*, 4090–4096.

[43] Zhang, C.; Tang, W.; Han, C. B.; Fan, F. R.; Wang, Z. L. Theoretical comparison, equivalent transformation, and conjunction operations of electromagnetic induction generator and triboelectric nanogenerator for harvesting mechanical energy. *Adv. Mater.* **2014**, *26*, 3580–3591.

[44] Han, C. B.; Jiang, T.; Zhang, C.; Li, X. H.; Zhang, C. Y.; Cao, X.; Wang, Z. L. Removal of particulate matter emissions from a vehicle using a self-powered triboelectric filter. *ACS Nano* **2015**, *9*, 12552–12561.

[45] Gu, G. Q.; Han, C. B.; Lu, C. X.; He, C.; Jiang, T.; Gao, Z. L.; Li, C. J.; Wang, Z. L. Triboelectric nanogenerator enhanced nanofiber air filters for efficient particulate matter removal. *ACS Nano* **2017**, *11*, 6211–6217.

[46] Pastoriza-Santos, I.; Liz-Marzán, L. M. Reduction of silver nanoparticles in DMF. Formation of monolayers and stable colloids. *Pure Appl. Chem.* **2000**, *72*, 83–90.

[47] Pastoriza-Santos, I.; Liz-Marzán, L. M. Formation of PVP-protected metal nanoparticles in DMF. *Langmuir* **2002**, *18*, 2888–2894.

[48] Zhao, X. L.; Wang, S.; Yin, X.; Yu, J. Y.; Ding, B. Slip-effect functional air filter for efficient purification of $PM_{2.5}$. *Sci. Rep.* **2016**, *6*, 35472.

[49] Zhu, G.; Chen, J.; Zhang, T. J.; Jing, Q. S.; Wang, Z. L. Radial-arrayed rotary electrification for high performance triboelectric generator. *Nat. Commun.* **2014**, *5*, 3426.

[50] Han, C. B.; Zhang, C.; Tang, W.; Li, X. H.; Wang, Z. L. High power triboelectric nanogenerator based on printed circuit board (PCB) technology. *Nano Res.* **2015**, *8*, 722–730.

[51] Kocik, M.; Dekowski, J.; Mizeraczyk, J. Particle precipitation efficiency in an electrostatic precipitator. *J. Electrost.* **2005**, *63*, 761–766.

[52] Xiao, G.; Wang, X. H.; Zhang, J. P.; Ni, M. J.; Gao, X.; Luo, Z. Y.; Cen, K. F. Granular bed filter: A promising technology for hot gas clean-up. *Powder Technol.* **2013**, *244*, 93–99.

[53] Liu, K. Y.; Rau, J. Y.; Wey, M. Y. Collection of SiO_2, Al_2O_3 and Fe_2O_3 particles using a gas-solid fluidized bed filter. *J. Hazard. Mater.* **2009**, *171*, 102–110.

[54] Chen, T. M.; Tsai, C. J.; Yan, S. Y.; Li, S. N. An efficient wet electrostatic precipitator for removing nanoparticles, submicron and micron-sized particles. *Sep. Purif. Technol.* **2014**, *136*, 27–35.

[55] Liu, C.; Hsu, P. C.; Lee, H. W.; Ye, M.; Zheng, G. Y.; Liu, N. A.; Li, W. Y.; Cui, Y. Transparent air filter for high-efficiency $PM_{2.5}$ capture. *Nat. Commun.* **2015**, *6*, 6205.

[56] Pline, W. A.; Lacy, G. H.; Stromberg, V.; Hatzios, K. K. Antibacterial activity of the herbicide glufosinate on *Pseudomonas syringae* pathovar glycinea. *Pestic. Biochem. Physiol.* **2001**, *71*, 48–55.

[57] de Oliva Neto, P.; Ferreira, M. A.; Yokoya, F. Screening for yeast with antibacterial properties from an ethanol distillery. *Bioresour. Technol.* **2004**, *92*, 1–6.

[58] Moritz, M.; Geszke-Moritz, M. The newest achievements in synthesis, immobilization and practical applications of antibacterial nanoparticles. *Chem. Eng. J.* **2013**, *228*, 596–613.

[59] Barani, H.; Montazer, M.; Samadi, N.; Toliyat, T. *In situ* synthesis of nano silver/lecithin on wool: Enhancing nanoparticles diffusion. *Colloids Surf. B* **2012**, *92*, 9–15.

[60] Agnihotri, S.; Mukherji, S.; Mukherji, S. Immobilized silver nanoparticles enhance contact killing and show highest efficacy: Elucidation of the mechanism of bactericidal action of silver. *Nanoscale* **2013**, *5*, 7328–7340.

[61] Tian, J. J.; Feng, H. Q.; Yan, L.; Yu, M.; Ouyang, H.; Li, H.; Jiang, W.; Jin, Y. M.; Zhu, G.; Li, Z. et al. A self-powered sterilization system with both instant and sustainable anti-bacterial ability. *Nano Energy* **2017**, *36*, 241–249.